International Journal of Heat and Mass Transfer 230 (2024) 125747

Contents lists available at ScienceDirect

International Journal of Heat and Mass Transfer

journal homepage: www.elsevier.com/locate/ijhmt

# Surface controlled mechanism of water boiling for nuclear reactor fuel assembly

A. Mokos [a,*], R.A. Patel [b], K. Karalis [c], S.V. Churakov [a,c], N.I. Prasianakis [a]

[a] Laboratory for Waste Management, Paul Scherrer Institute (PSI), Villigen 5232, Switzerland
[b] Institute of Concrete Structures and Building Materials, Karlsruhe Institute of Technology, Germany
[c] Institute of Geological Sciences, University of Bern, Switzerland

ARTICLE INFO

*Keywords:*
Cross-scale
Modelling
Multiphase simulations
Bubble nucleation site density
Boiling water reactor
Lattice-Boltzmann
Molecular dynamics

ABSTRACT

The mechanism of bubble nucleation in boiling water at solid surface remains poorly understood. In this study, the water boiling and bubble nucleation density under nuclear reactor operation conditions were investigated by multiphase Lattice Boltzmann and Molecular Dynamics simulations. The developed multiscale model takes into account the surface energy of $ZrO_2$ cladding in different crystallographic planes obtained by molecular dynamics simulations and uses it to inform the corresponding contact angle of two-phase fluid in the thermal multiphase Lattice Boltzmann model. The model describes the bubble formation on a rough surface due to boiling and predicts the number of active nucleation sites on surfaces of different roughness. Further, the effect of the different contact angles on bubble dynamics while in close contact with the surface is investigated. The obtained results are in good agreement with experimental observations and provide functional relationships between interface properties (roughness, surface energy) and the nucleation site density, necessary for macroscopic simulations of the boiling phenomena.

## 1. Introduction

The phase change of water from liquid to vapour at boiling conditions is one of the main mechanisms controlling the heat and mass transfer within working and cooling fluid of nuclear reactor systems. Despite the extensive use of water as a coolant in nuclear reactors, both in boiling water reactors (BWR) and in pressurized water reactors (PWR), the heterogeneous nucleate boiling mechanism and its interplay with the cladding surface is still not sufficiently understood. This is particularly important within the fuel assembly (FA) systems, where exceeding the critical heat flux on the surface can lead to inefficient heat transfer and increased thermal fatigue through the 'boiling crisis' phenomenon. At these conditions, steam forms a layer above the cladding surface, increasing its temperature locally [1].

In addition, the boiling mechanism is controlling the build-up of deposits (commonly referred to as crud) around the fuel rods, which may lead to significant deviations from the expected power output [2,3]. Surface crud deposition is also of major safety concern [4], as such layers alter the heat resistance of the cladding, potentially reducing heat exchange between the fuel and the coolant, affecting the safe operation of the powerplant [5] and resulting eventually in a more frequent maintenance interval. It is therefore imperative to understand the boiling mechanism within the reactor, particularly the transition between nucleate and pool boiling. In this study, we investigate the processes of boiling nucleation, at the interface between the coolant and the cladding, following a multiscale modelling approach.

For the FA systems considered here, the external surface of the fuel rod (the cladding) consists of $ZrO_2$, commonly referred to as zirconia. It is formed due to corrosion of the zirconium alloys composing the cladding. The oxidation occurs during the earlier stages of the fuel rod submergence in the reactor and leads to the growth of uniform oxide films [6].

While experiments have been carried out [7,8], the radioactive nature of the materials and the pressure and temperature conditions make the in-situ studies of bubble nucleation a very challenging task. For that reason, semi-empirical [1,9] and numerical approaches [10,11] have been employed to predict the nucleation boiling characteristics. For the latter, the current state of the art focuses on the macroscopic scale, using interface methods to track the interaction between gas and liquid and numerical models to investigate smaller scales [11,12]. However, boiling is in fact a multiscale phenomenon, as the water molecule density first starts decreasing in the molecular scale ($10^{-10}$ to $10^{-9}$m) and

* Corresponding author.
*E-mail address:* athanasios.mokos@psi.ch (A. Mokos).

https://doi.org/10.1016/j.ijheatmasstransfer.2024.125747
Received 19 December 2023; Received in revised form 16 April 2024; Accepted 19 May 2024
Available online 30 May 2024

the bubbles are generated in the microscale ($10^{-6}$ to $10^{-5}$m), before interacting with the main water flow in the macroscale ($10^{-3}$ to $10^{2}$m). While MD and atomistic descriptions provide the basic understanding of the boiling phenomena, it is computationally unfeasible to conduct MD simulations at the micrometre level, both due to the large number of atoms needed to be considered and due to the longer timescales [10].

In our previous study [13] we investigated the heterogeneous bubble nucleation on nanoscale $ZrO_2$ surfaces using the transition path sampling (TPS) method [14] and Molecular Dynamics (MD) modelling. The present paper relies on the results of the atomistic simulations and describes the evolution of two-phase boiling system with the Lattice Boltzmann (LB) approach, where statistic representations of particles are considered, bridging molecular and pore scale approaches. The LB approach was selected due to its ability to capture mesoscopic phenomena and the accuracy and ease of use when capturing both gas-liquid interfaces and phase change in simple or complex geometries [15,16]. It has also been successfully applied to simulate the boiling process [17], and can take the surface roughness explicitly into account.

In this paper the nanoscale MD simulations of vapour bubble on the surface of cladding were used to determine the contact angle between the three phases: vapour bubble, water liquid and solid zirconia surface based on the interatomic interaction potentials. The contact angles depend on the crystallographic structure and orientation of zirconia surface. The contact angle, which expresses the interaction of gas-fluid-solid at the atomic scale, is the upscaling parameter, serving as input to microscale LB simulations and controlling the fluid-solid interactions.

The microscale simulations with a developed LB multiphase model are used to investigate the effect of different contact angles on the behaviour of droplets and bubbles on an inclined or flat surface. Both static (resting until equilibrium) and dynamic cases (bubble entry into domain) are considered. The flow of a bubble over rough surfaces, generated through fractal functions, is also considered.

The model is further applied to study the onset of boiling by explicitly considering the effect of surface roughness. The evolution of newly created bubbles is considered on both flat (produced at predetermined positions) and at rough surfaces (produced through the temperature differences caused by the surface troughs and peaks). It is then possible to estimate the nucleation site density for a given surface roughness and for a given material which in this case is zirconia at BWR conditions.

## 2. Molecular scale methods and simulations

### 2.1. Methodology

The equilibrium shape and contact angle of vapour bubble on zirconia surface was obtained by classical molecular dynamics (MD) simulations using the LAMMPS v.2019 code [18]. A non-polarizable SPC/E model and classical FF for $ZrO_2$ applied here was benchmarked in our previous study [19]. The cross interaction between water and solid described by the Lorentz-Berthelot mixing rule was utilized for the unlike Lennard-Jones parameters [20]. Two different crystallographic orientations $(\bar{1}11)$ and $(001)$ zirconia were investigated [13,21]: $(\bar{1}11)$ surface with hydrophilic properties and $(001)$ surface exhibiting slightly hydrophobic properties.

The supercell (see Fig. 1) consisted of 3380 $H_2O$ and 1024 $ZrO_2$ molecules. The contact angles at temperature 568 K and pressure 80bar (following the BWR in-situ operating conditions mentioned in the introduction) were calculated using the Young-Dupré equation:

$$W_{sl} = \gamma_{lv}(1 + \cos\theta), \tag{1}$$

where $W_{sl}$ is the work of adhesion, $\gamma_{lv}$ is the liquid-vapor surface tension and $\theta$ is the contact angle. The pressure in the simulations was controlled by utilizing a piston, which acted as a barostat. This approach was employed to eliminate periodicity in the z-direction, thereby discarding unnecessary electrostatic interactions between real and replica simulation cells in that direction.

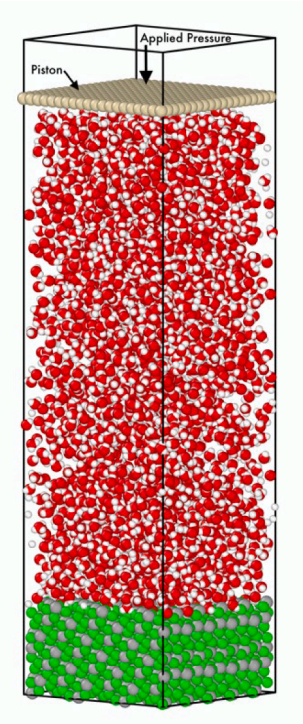


**Fig. 1.** A snapshot of molecular dynamics simulations of the zirconia-water interface at 568K and 80 bar. The pressure was regulated using the piston, with particular emphasis on the supercell length in the z-direction ensuring the periodicity elimination. The oxygen atoms of the zirconia are green, the zirconium atoms are grey, and the oxygen and hydrogen atoms of water are red and white, respectively.

### 2.2. Mechanism of bubble emergence and measurement of contact angle

The contact angle of a vapour bubble and the surface functionality are strongly related to each other, and therefore the contact angle needs to be computed for both $(\bar{1}11)$ and $(001)$ planes. From the molecular scale perspective, the bubble nucleation is a rare event associated with a large activation energy barrier, whose mechanism was studied with the TPS method. Fig. 2 shows a series of snapshots illustrating the vapour bubble nucleation obtained by MD simulations. The bubble is separated from the zirconia surface with a thin water layer about 7 Å thick as consequence of the surface hydrophilicity.

Large-scale MD simulations were applied to simulate the equilibrium shape of the vapour bubble at the surface and to derive the contact angles (see Fig. 2). The contact angle of the hydrophobic interface plane is 71.6° while for the hydrophilic $(\bar{1}11)$ interface a large work of adhesion (see Fig. 3) value was obtained indicating a complete wetting (zero contact angle). Fig. 3 shows the average Hamiltonian derivatives together with the work of adhesion calculated according to the Young-Dupré equation (Eq. (1)). For both the hydrophobic and hydrophilic interfaces, the work of adhesion increased with strengthening of the solid-liquid interaction as expected. This results in increasing wettability as shown in Fig. 3(b) and decreasing contact angle [22].

This approach provides several advantages compared to the traditional method of developing bubbles since the supercell is in a steady state, the pressure is maintained through a piston, and there is no physical bubble in the domain, suggesting that no dynamic processes will occur during the simulation like bubble growth/collapse.

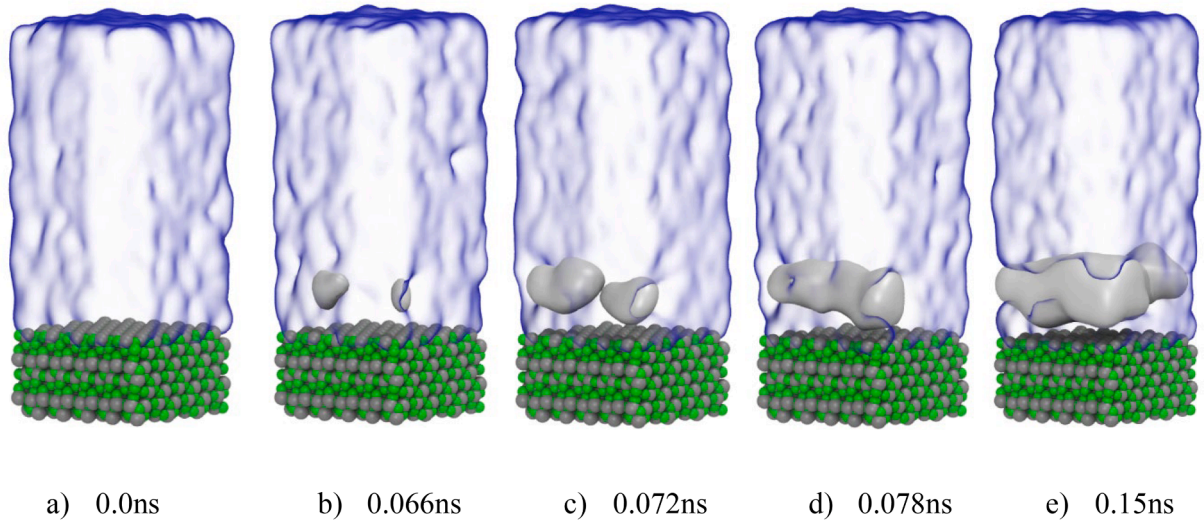


**Fig. 2.** A time series of snapshots from MD simulation illustrating heterogeneous nucleate boiling in contact with the $(\bar{1}11)$ plane. Two bubbles are nucleated (b) and grow (c) until they merge (d) to form a void layer (e).

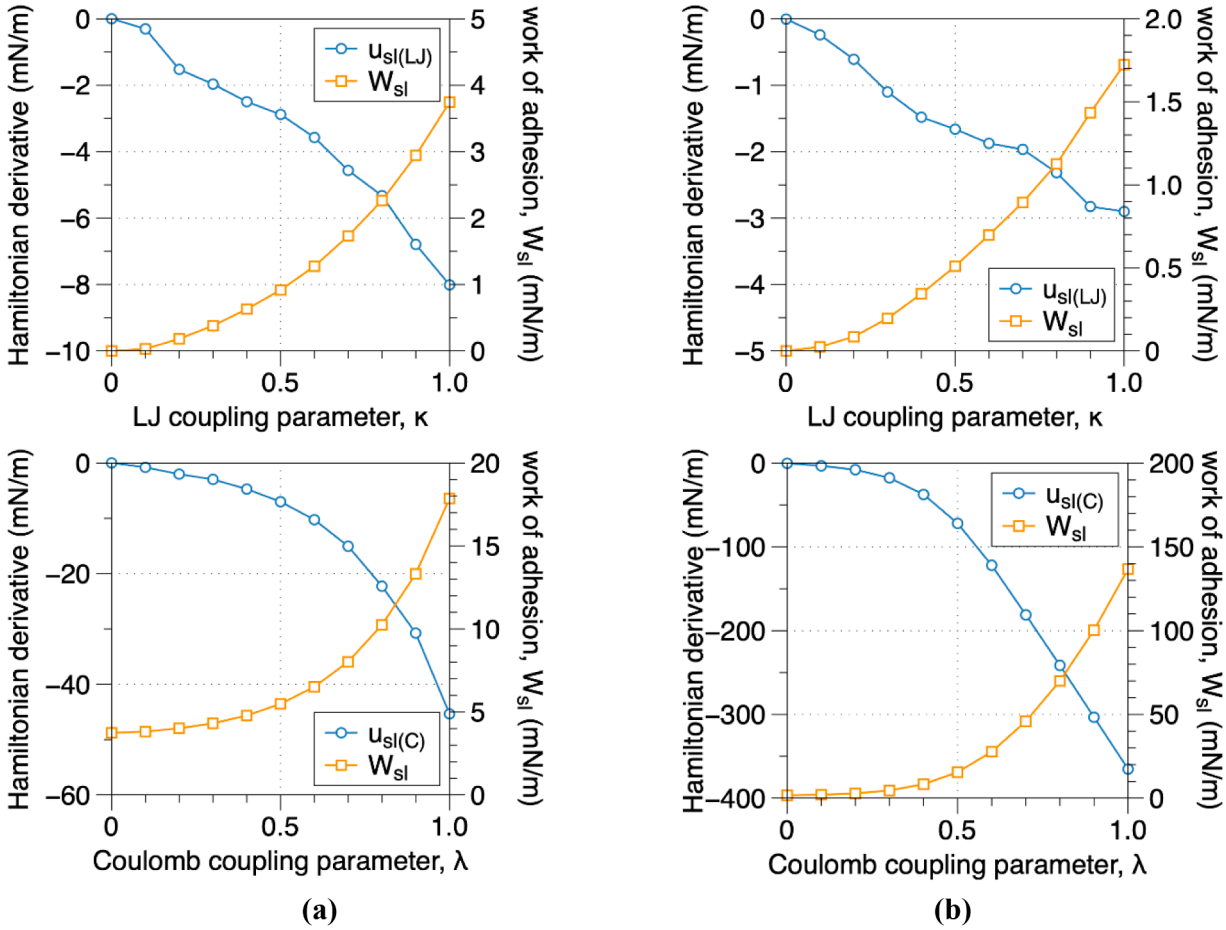


**Fig. 3.** Average of Hamiltonian derivatives ($U_{sl(LJ)}$ and $U_{sl(C)}$) and work of adhesion ($W_{sl}$) for (a) the hydrophobic (001) interface and (b) the hydrophilic $(\bar{1}11)$ interface at 568K and 80 bar. The value of the work of adhesion ($W_{sl}$) at k = 1, for the Lennard Jones coupling parameter case serves as the starting point for evaluation the work of adhesion using the Coulomb coupling parameter. The cumulative $W_{sl}$ at λ equal to 1.0 of the Coulomb coupling parameters is employed in the Young-Dupré equation to calculate the water contact angle.

## 3. Microscale level methods and simulations

The developed LB flow and multiphase models are implemented within the open source code framework Yantra [23]. An additional thermal model has been added to the code, for which validations are provided in Appendix A.

### 3.1. Lattice Boltzmann framework for the momentum equations

The LB numerical framework is based upon the solution of the discretised Boltzmann equation with simplified collision models to recover correct macroscopic behaviour. Under the asymptotic limit Navier-Stokes (NS) equations (momentum and continuity) can be recovered from the lattice Boltzmann equation through a multi-scale Chapman-Enskog expansion [24–26]. The incompressible NS equation for the momentum which is recovered for Mach numbers below the incompressiblity limit is shown here:

$$\frac{\mathrm{d}\boldsymbol{u}}{\mathrm{d}t} = -\frac{1}{\rho}\nabla p + \nu\nabla^2\boldsymbol{u} + \boldsymbol{G} \tag{2}$$

where u is the velocity vector, the fluid density, p the pressure, the kinematic viscosity and G an external force (gravity).

The discretised LB method describes the evolution of a particle distribution function $f$ on a regularised lattice. In this paper, the D2Q9 lattice is used for 2D simulations, meaning that the distribution function and the particle velocities will be discretised along 8 lattice directions and one rest node, taking the forms $f_i$ and $\boldsymbol{c}_i$, $i = 0\ldots8$, respectively. The discretised velocities for the D2Q9 matrix on a regular lattice can be written as [27]:

$$\boldsymbol{c}_i = \begin{cases} (0,0), \text{ if } i = 0 \\ \left(\cos\left(\frac{(i-1)\pi}{2}\right), \sin\left(\frac{(i-1)\pi}{2}\right)\right), \text{ if } i = 1-4 \\ \sqrt{2}\left(\cos\left(\frac{(i-5)\pi}{2}+\frac{\pi}{4}\right), \sin\left(\frac{(i-5)\pi}{2}+\frac{\pi}{4}\right)\right), \text{if } i = 5-8 \end{cases} \tag{3}$$

To model the particle collisions, a two-relaxation-time (TRT) variant of the LB method is considered [28,29]. Among several options, the TRT model was selected due to its increased stability without introducing numerical complexity [29]. In the TRT variant, the symmetric (indicated by a "+" superscript) and antisymmetric parts (indicated by a "–" superscript) are defined such that the odd moments of the symmetric and the even moments of the antisymmetric parts are zero, as shown in Eq. (4).

$$f_i^+ = \frac{f_i + f_{\bar{i}}}{2}, \; f_i^- = \frac{f_i - f_{\bar{i}}}{2} \tag{4}$$

The main LB equation for the update of the distribution function for the TRT model in both space and time for the NS equations is shown in Eqs. (5) and (6) [28]. The mass and momentum equations, including phase change, are solved using one set of distribution functions, while the temperature dynamics are solved using a separate set, as shown in Section 3.2.

$$f_i(\boldsymbol{r} + \boldsymbol{c}_i\,\Delta t,\; t + \Delta t) - f_i(\boldsymbol{r}, t) = \Delta t\Omega_i^{TRT}(\boldsymbol{r}, t) \tag{5}$$

$$\Omega_i^{TRT}(\boldsymbol{r}, t) = -\frac{1}{\tau^+}\left(f_i^+(\boldsymbol{r}, t) - f_i^{eq+}(\boldsymbol{r}, t)\right) - \frac{1}{\tau^-}\left(f_i^-(\boldsymbol{r}, t) - f_i^{eq-}(\boldsymbol{r}, t)\right) \tag{6}$$

In Eq. (5), $\tau$ denotes the LB relaxation time while $f^{eq}$ is the equilibrium distribution. For the TRT scheme, two numerical relaxation times are used. Their value is not independent but are connected through an empirical magic parameter $\Lambda$ as shown in Eq. (7) [28]. The value of the latter can be determined through stability analysis [29]. This leaves one relaxation time as a free parameter depending on the case. For the NS equations, the symmetric relaxation time $\tau^+$ will be determined according to the fluid viscosity as shown in Eq. (9).

$$\Lambda = (\tau^+ - 0.5)(\tau^- - 0.5) \tag{7}$$

The equilibrium distribution is given by a Taylor series expansion of the Maxwell-Boltzmann distribution up to second order [30] as shown in Eq. (8). The equation is connected to the universal gas constant through the speed of sound $c_s$. For a regular D2Q9 lattice, the speed of sound is $c_s = 1/\sqrt{3}$ and is related to the gas constant as $c_s^2 = RT_L$, where $R$ is the universal gas constant and $T_L$ is the lattice temperature (equal to 1/3). The Maxwell-Boltzmann distribution can then be written as an equation of the speed of sound.

$$f_i^{eq} = w_i\rho\left(1 + \frac{\boldsymbol{c}_i\cdot\boldsymbol{u}_i}{c_s^2} + \frac{(\boldsymbol{c}_i\cdot\boldsymbol{u}_i)^2}{2c_s^4} - \frac{\boldsymbol{u}_i\cdot\boldsymbol{u}_i}{2c_s^2}\right) \tag{8}$$

The term $w_i$ is the weight of the discrete velocity $c_i$. For the D2Q9 lattice, these are $w_0 = \frac{4}{9}$, $w_{1-4} = \frac{1}{9}$ and $w_{5-8} = \frac{1}{36}$.

The particle distribution function is used to recover the macroscopic properties of the fluid as shown in Eq. (9) for the velocity and density in the D2Q9 lattice. The fluid viscosity is also linked to the LB relaxation time, as previously mentioned.

$$\boldsymbol{u} = \frac{1}{\rho}\sum_{i=0}^{8} f_i\boldsymbol{c}_i, \;\; \rho = \sum_{i=0}^{8} f_i, \;\; \mu = (\tau^+ - 0.5\Delta t)T_L \tag{9}$$

To simulate the interface between the gas and liquid phases, the Shan-Chen (SC) interface force is used [31,32]. This adds a source/sink term to the collision factor $\Omega$, generating an attractive force between the node under consideration and its nearest neighbours. Eq. (10) describes the force term for the D2Q9 lattice.

$$F_c(\boldsymbol{r}, t) = -G\psi(\boldsymbol{r}, t)\sum_{i=1}^{8} w_i\psi(\boldsymbol{r} + \boldsymbol{c}_i\Delta t, t)\boldsymbol{c}_i \tag{10}$$

The variable $G$ is an empirical parameter controlling the strength of the forcing term and $\psi$ is the mean-field potential. A value of -1 is used for the parameter. To calculate the potential, the function, shown in Eq. (11) and proposed by [33], is used to maintain thermodynamic consistency. The equation is coupled with a non-ideal equation of state (EOS) to compute the pressure and connect the thermodynamic quantities of the fluid.

$$\psi(\rho) = \sqrt{\frac{2\left(P_{eos}(\rho, T) - c_s^2\rho\right)}{c_s^2 G}} \tag{11}$$

The present paper uses the Peng-Robinson (PR) EOS [34] as it provides reasonable accuracy near the critical point [35], which is very close to the conditions within the NPP cooling system. The PR EOS is shown in Eq. (12) and is expressed in terms of the critical temperature $T_c$ and pressure $p_c$, as well as the acentric factor $\omega$.

$$\begin{gathered} P_{eos}(\rho, T) = \frac{\rho RT}{1 - b\rho} - \frac{a\phi(T)\rho^2}{1 + 2b\rho - b^2\rho^2} \\ \phi(T) = \left(1 + \left(0.37464 + 1.54226\omega - 0.26992\omega^2\right)\left(1 - \sqrt{T/T_c}\right)\right)^2 \\ a = 0.45724\frac{R^2T_c^2}{p_c}, \;\; b = 0.07780\frac{RT_c}{p_c} \end{gathered} \tag{12}$$

Unless mentioned otherwise, the following parameters are used for the Peng-Robinson equation: $a = \frac{2}{49}$, $b = \frac{2}{21}$ and $\omega = 0.3443$. To incorporate the forcing term in the main LB equation, rather than incorporate an additional term in Eq. (5), the fluid velocity is directly modified by Eq. (13) as suggested by [36]. The modified velocity $\boldsymbol{u}^*$ will then be used in Eqs. (6) and (8).

$$\boldsymbol{u}^* = \boldsymbol{u} + \frac{F_c\tau^+}{2\rho} \tag{13}$$

### 3.2. Lattice Boltzmann framework for the thermal equations

To solve the energy field, the LB method is used to solve the convection-conduction equation. The exact equation for a non-ideal gas system, expressed via the temperature $T$ and the specific volumetric heat capacity $C_V$ can be written as:

$$\rho C_V\left(\frac{\partial T}{\partial t}+\boldsymbol{u}\cdot\nabla T\right)=\nabla\cdot k\nabla T-T\left(\frac{\partial p}{\partial T}\right)_{\rho}\nabla\cdot\boldsymbol{u}+O(\boldsymbol{u}^2) \tag{14}$$

where $k$ is the thermal conductivity. Assuming a linear equilibrium and an orthogonal lattice is used,Eq. (14) can be simplified to Eq. (15) [37]:

$$\frac{\partial T}{\partial t}+\nabla\cdot\boldsymbol{u}T=\nabla\cdot\lambda\nabla T+S+O(\boldsymbol{u}^2),\ \lambda=\frac{k}{\rho C_V} \tag{15}$$

In this equation, $\lambda$ is the thermal diffusivity and $S$ is a source-sink term, shown in Eq. (16), to solve the additional terms occurring from the simplification of Eq. (14) to simulate the liquid vapour phase change. The source-sink term consists of two parts, the first of which is solved using the Peng-Robinson gradient and the second is solved using a second order finite difference scheme [38]. The thermal diffusivity is connected to the relaxation time of the TRT scheme as follows: $\lambda=(\tau^{-}-0.5\Delta t)T_L$.

$$S=T\left(1-\frac{1}{\rho C_V}\left(\frac{\partial p}{\partial T}\right)_{\rho}\right)\nabla\cdot\mathbf{u}-\mathrm{k}\nabla\mathrm{T}\cdot\nabla\left(\frac{1}{\rho C_V}\right) \tag{16}$$

For the LB model, the temperature dynamics in Eq. (15) are solved using a separate second distribution function $g$, using the D2Q5 lattice. This lattice also uses the TRT scheme and therefore can be described through the same Eqs. (5) and (6). It is used due to its robustness and accuracy in low Péclet numbers compared to the D2Q9 lattice for the thermal equation [39]. The source-sink term is then added to the collision factor as a separate term.

The scheme connecting the momentum and thermal equations is usually referred to as the double distribution function (DDF) scheme. The thermal and momentum equations are executed independently of each other but are coupled via the equation of state and the macroscopic quantities: the temperature is passed from the energy to the momentum equation while the velocity and density are passed to the energy from the momentum equation. A two-way coupling can then be established.

For the equilibrium distribution function, a modified Eq. (8) using only the linear part of the Maxwell-Boltzmann distribution (the first term within the parenthesis) will be utilised. The quadratic velocity terms are not needed, as they are not contained in the convection-conduction equation [40].

The model presented here is implemented within the open source LB framework Yantra [23], which has already been validated for the solution of the momentum and diffusion equations [37,41]. The validations for the thermal model are shown in Appendix A, covering a conjugate heat transfer and a differentially heated cavity.

More relevant to this problem as a validation case is a Stefan problem for a one-dimensional phase change simulation, shown in Fig. 4. The domain consists of water at both vapour and liquid phases. Each phase has different temperatures as shown in Fig. 4 with a vapour density of 0.318 and density ratio of 20. As the simulation advances, the liquid temperature slowly increases and the water phase changes to vapour. The position $s$ of the interface between the two phases can be found through an analytical relation shown inEq. (17), where $\beta$ is the Stefan number.

$$s(t)=2\zeta\sqrt{\lambda t}\ \text{where}\ \zeta\ \text{satisfies}\ \beta\zeta=\frac{e^{-\lambda^2}}{\sqrt{\pi}\mathrm{erf}\zeta} \tag{17}$$

The interface in the LB simulation can be easily tracked through the fluid density, as shown in Fig. 4(a). The transcendental Eq. (17) is solved using the *fsolve* function of the SciPy Python library. Fig. 4(b) shows the comparison between the analytical and LB results. The simulation shows very good agreement to the theoretical values. It is likely the difference is due to the finite domain of the simulation, creating boundary effects, as the analytical solution is only valid for an infinite domain.

### 3.3. Non-dimensionalisation of Lattice-Boltzmann model

This study investigated water boiling at the in-situ conditions of a BWR. The pressure within the system is considered to be 80 bar, with a density ratio of 17.034 and a temperature of 295°C, which is 87 % of the critical temperature. A uniform heat flux of 500,000 W/m$^2$ is assumed between the walls and the coolant. For simplicity, the coolant is also assumed to be pure water. The thermodynamic properties of water in liquid and vapour phase, including diffusivity, surface tension, etc. were obtained using the Coolprop library [42].

The LB framework solves the equivalent problem via proper dimensionalisation of physical units, where one lattice unit (LU) is equivalent to 1 μm. The similarity is achieved through maintaining the value of the dimensionless numbers. In particular, three dimensionless numbers are considered here: (a) the Prandtl number *Pr*, which allows to define the thermal diffusivity in LB units; (b) the Laplace number *La*, which allows to define the surface tension coefficient value and c) the Eötvös number *Eo*, which allows to define the gravity time step in lattice Boltzmann units. Eq. (18) shows the mathematical expressions of the relevant dimensionless numbers:

$$Pr=\frac{c_p\mu}{k},La=\frac{\sigma\rho L}{\mu^2},Eo=\frac{\Delta\rho gL^2}{\sigma}, \tag{18}$$

where $c_p$ is the specific heat, $\sigma$ is the surface tension between liquid and vapour and $L$ is the characteristic length. The water and vapour properties are computed through the Coolprop library, so the Prandtl value is 0.879. The LB time step therefore corresponds to 30.7ns per LB time step. The liquid-vapour density ratio is also maintained throughout the simulations and is equal to 17.034, which corresponds to the system pressure and temperature.

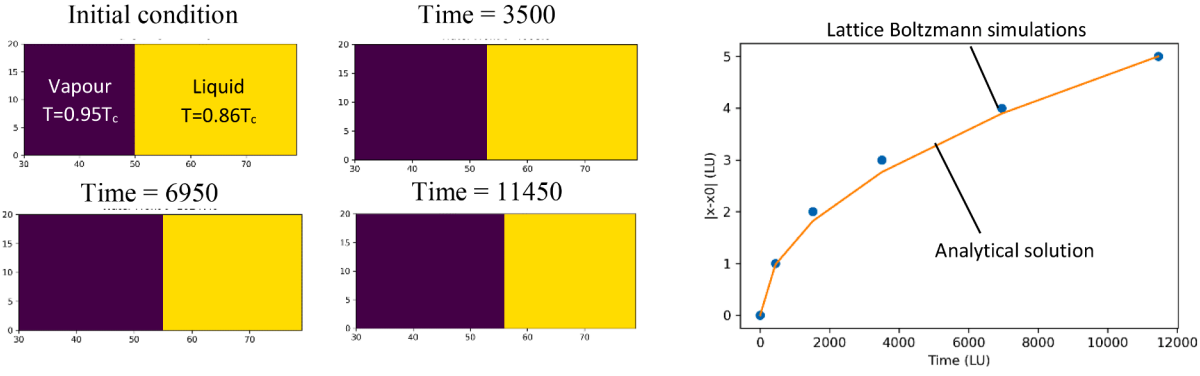


a) Evolution of the domain density

b) Comparison between analytical and simulation results

**Fig. 4.** LB results for a one-dimensional boiling simulation, showing the time evolution of the interface(left) and comparison with analytical results (right).

Since the simulations need to be able to model the emergent bubbles, the specific dimensionalisation was selected based on the predicted size of the bubble departing from the surface, as computed for the specific conditions using the empirical relations derived by [9] with a value of 7.7μm. The bubble departure diameter is also used as the characteristic length for the calculation of the Laplace and Eötvös numbers, with values of 1120 and $2.53{\cdot}10^{-5}$, respectively. A minimum of 5 LB cells is required to achieve sufficient accuracy in modelling the departing bubble. Therefore, the similarity selected is that the node distance between two LB nodes would correspond to $10^{-6}$m. This allows nearly 8 cells to be used across the bubble diameter which should be sufficient for its modelling. Appendix B shows a grid refinement study showcasing that the current grid is sufficient for the simulations considered here.

Table 1 shows the correspondence of the basic values between the LB simulation and the real case. These are obtained by the similarity processes outlined previously, in addition to some LB parameters whose value was selected based on previous work [17,38]. These parameters are the LB viscosity, set to 0.5/3, the LB vapour density, set to 0.318 and the LB specific heat capacity, which corresponds to 6. The value of the magic parameter $\Lambda$ is 0.25 for the momentum (whereupon $\tau^+ = \tau^-$) and 0.1875 for the thermal calculations.

Of particular interest is the interaction at the interface between the solid and the fluid. Applying a mechanical equilibrium at the boundary position, the density profile of the boundary can be imposed [43] so that $\psi\left(\rho\left(x_{boundary}\right)\right) = \psi(\rho_w)$ where the wall density $\rho_w$ is an empirical parameter not connected to the actual value of the solid density. In this paper, the value of the wall density will be used to adjust the contact angle between the boundary and the fluid phases.

A test case of a droplet/bubble in equilibrium on a flat surface is used to calibrate the wall density. As expected, and as shown in Fig. 5, adjusting the model parameter $\rho_w$ that is used to control the contact angle, leads to different behaviour of the droplet/bubble. As the droplet achieves equilibrium, the contact angle with the solid boundaries can be measured through the area of the resulting spherical cap [44]. Through multiple cases with different wall densities, an empirical relation can be found with the contact angle. For the specific dimensionalisation used in this paper, the relation was found to be approximately linear and is given as:

$$\theta = -27.643\rho_w + 173.86 \text{ with } R^2 = 0.9581 \tag{19}$$

### 3.4. Effect of surface characteristics due to contact angle variation

Having defined all the relevant fluid parameters in the LB simulation, the interaction with the zirconia surface, governed by the wall density $\rho_w$, also needs to be computed. The MD simulations in Section 3 showed that the zirconia has different crystallographic orientations that lead to different contact angles with the water. Both surfaces, $(001)$ and $(\bar{1}11)$, were investigated, as their different properties are expected to influence the fluid-solid interactions and to lead to different behaviour for the fluid at the microscale.

**Table 1**
LB dimensionalisation data for BWR conditions.

| Physical Parameter | Real value | LB Value |
|---|---|---|
| Node distance | $10^{-6}$m | 1 |
| Eötvös number | $2.53{\cdot}10^{-5}$ | $2.53{\cdot}10^{-5}$ |
| Prandtl number | 0.879 | 0.879 |
| Laplace number | 1120 | 1120 |
| Temperature ratio | 0.878 | 0.878 |
| Superheat | 8°C | $9.02{\cdot}10^{-4}$ |
| Vapour density | 42.4kgm$^{-3}$ | 0.318 |
| Liquid density | 722.24kgm$^{-3}$ | 5.417 |
| Density ratio | 17.034 | 17.034 |
| Thermal conductivity (liquid) | 0.56034Wm$^{-1}$K$^{-1}$ | 1.14 |
| Gravity force | 9.81ms$^{-2}$ | $9.22{\cdot}10^{-9}$ |

Using the relation for the contact angles, we can identify the corresponding density values: (a) 6.3 for the $ZrO_2$ $(\bar{1}11)$ surface at BWR conditions, (b) 4.95 for the $ZrO_2$ $(\bar{1}11)$ surface at atmospheric conditions and (c) 3.1 for the $ZrO_2$ $(001)$ surface at BWR conditions. These angles can be seen in Fig. 5. For the $(\bar{1}11)$ surface, as the angle is too small to be measured with the MD simulations, we are using the smallest angle that can be detected with the spherical cap approach for this specific dimensionalisation at 7.5°. To validate these results, static bubble simulations using the same starting conditions were conducted. As shown in Fig. 5, where the bubble has reached its steady state, the equivalent contact angles were achieved. Note that only the results from Fig. 5(a) and (c) are used in the subsequent simulations; Fig. 5(b) serves as a validation case for Eq. (19).

### 3.5. Hydrodynamic behaviour due to contact angle variation

While the bubble equilibrium on a flat surface is explainable by the contact angle, it is interesting to investigate the dynamic behaviour of a droplet placed between two inclined surfaces similar to a surface micrometre-size dent. Fig. 6 shows the position of a bubble at equilibrium after being placed at a 60° incline within a triangular trough. For the $(\bar{1}11)$ surface, the droplet equilibrates at the bottom of the trough exposing a concave free surface. For the $(001)$ surface, the droplet also equilibrates at the bottom, however, the exposed surface is convex, limiting the contact surface with the side walls. The final contact angles of the bubbles in Fig. 6(b) and (c) are similar to the bubbles in Fig. 5(b) and (c), respectively, meaning that the surface orientation does not affect the wall density. The gravity field is not considered in these simulations and the dynamic process is governed solely by the vapour-liquid-solid interactions. Note that contact angle hysteresis [45] will not be explicitly considered in this paper as we expect very little influence on the movement of the bubbles across the surface compared to the considered mechanisms.

The setups explored so far start from an initial configuration and equilibrate in a dynamic way in closed systems without pressure gradients driving the flow. It is interesting to investigate these interactions in a more dynamic environment with open boundaries. Fig. 7 shows a dynamic regime, where vapour is inserted through an orifice (5LU/5μm width) in an initially still liquid domain. The orifice is treated as an open boundary containing air. Applying the equation of state across all particles leads to a pressure gradient near the orifice due to the density ratio, which leads to the gradual insertion of air in the domain. An open boundary with zero velocity is imposed at the top, with periodic boundaries along the domain height. The open boundaries along the top and bottom, coupled with the pressure gradient near the orifice, lead to the influx of vapour in the domain.

As the vapour volume increases, a bubble is formed near the orifice. However, the size of the resulting bubble, its shape and its interaction with the wall differs depending on the contact angle. As shown in Fig. 7 (a and b), the bubble forms a spherical shape for the $ZrO_2$ $(\bar{1}11)$ surface after 40,000 LB time steps (corresponding to 1.223ms) but its contact surface with the wall is larger compared to the generic wall with the smaller contact angle. For the $ZrO_2$ $(001)$ surface at Fig. 7(c), the bubble has a semi-circular shape and remains in close contact with the solid surface. The interaction of a moving bubble through an orifice and particularly its shape has implications important for boiling within the FA systems, since close contact of moving vapour bubbles with the surface for longer periods could promote more frequent dry out conditions accompanied by local increase in wall temperature and potential micro-damage on the cladding.

It is very interesting to observe the predictions of the model for the bubble behaviour when the geometry around the orifice changes. Fig. 8 shows the position and evolution of the bubble at the same time as Fig. 7. The orifice is now placed within a 45° inclined surface. Owing to the increased contact with the solid surface and therefore the increased

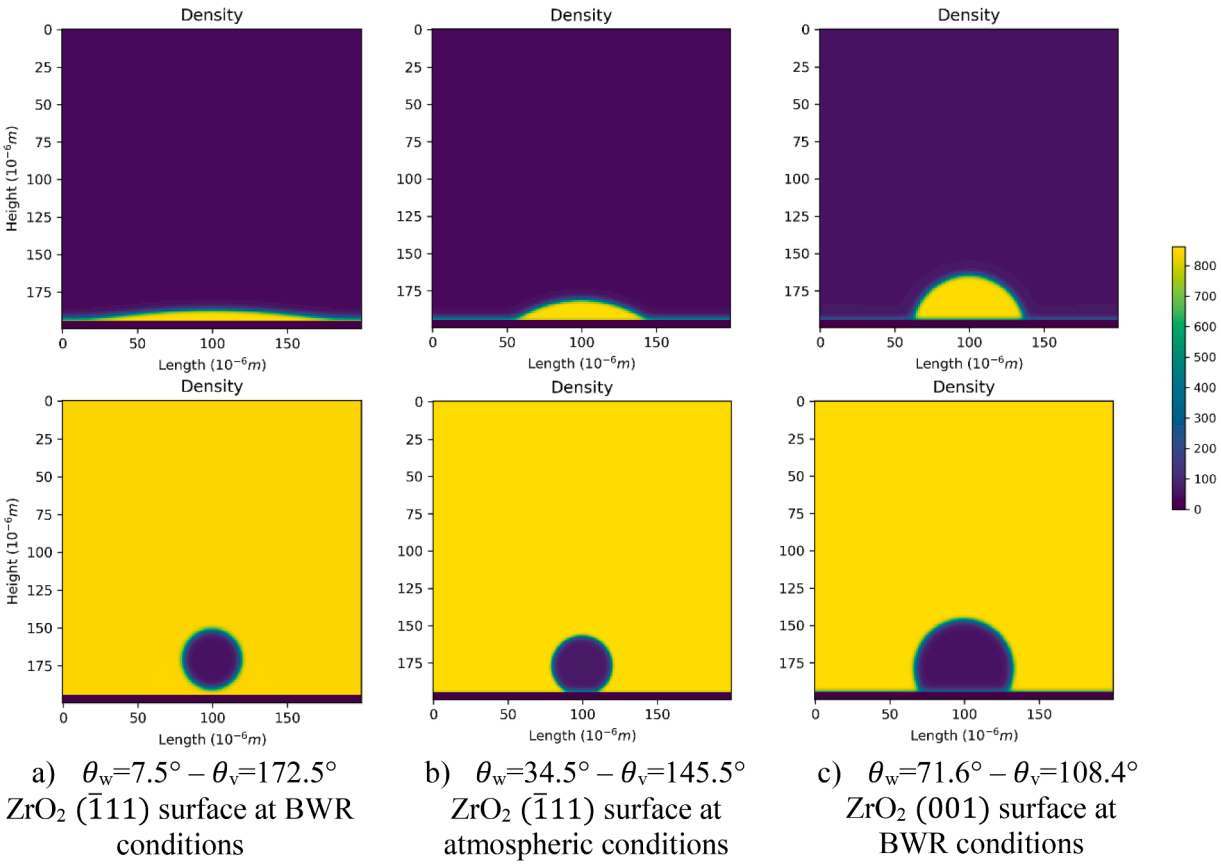


**Fig. 5.** Contact angles for droplets (top row) and bubbles (bottom row) for different interface planes: (a) the $ZrO_2$ plane at BWR conditions, (b) the $ZrO_2$ ($\bar{1}11$) plane at atmospheric conditions and (c) the $ZrO_2$ (001) plane at BWR conditions.

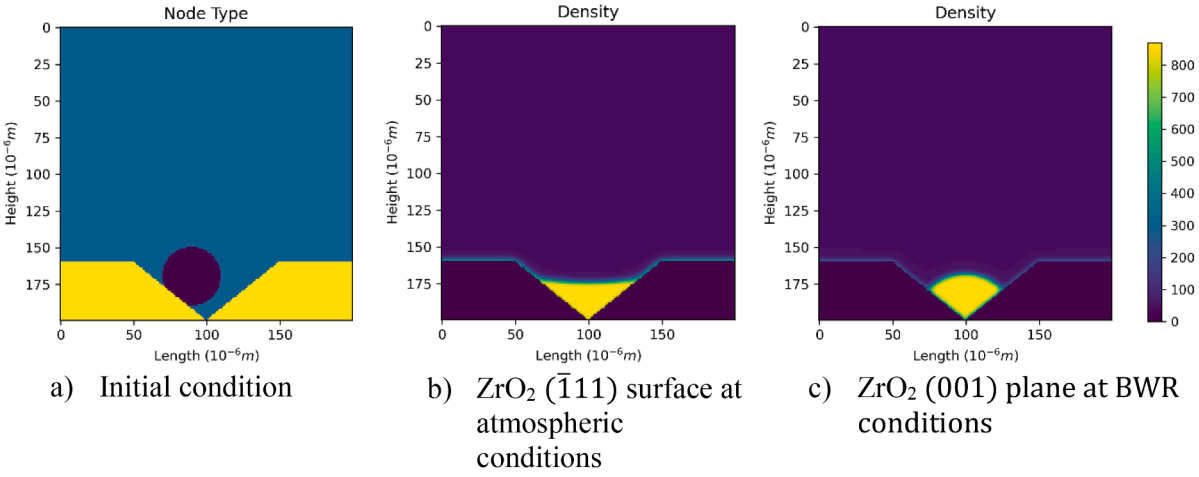


**Fig. 6.** Contact angles for droplets at a 60° incline for different $ZrO_2$ interface planes.

effect of the contact angle compared to Fig. 7, their vapour bubble volumes are very different, with the (001) plane bubble showing the smallest size and maintaining more contact with the solid boundary. Their shape also seems to impede liquid volume exchange with the main flow, which could indicate a higher potential of a dry out phenomenon.

### 3.6. Vapour-liquid-solid interactions over a rough surface

The showcases presented in the previous section indicate that the surface micro-roughness may play a significant role in the boiling process. Naturally, the surface profile of the cladding will differ depending on the manufacturer and the plant specifications. To create a more generalised model, algorithmically computer-generated surfaces will be used for the simulations in this section, with the methodology of course still applicable on experimentally measured profiles.

To create the surface roughness, the method of [46] as applied by [47] is used. In more detail, fractal geometries were generated by overlaying a series of sine waves with random phase but the same amplitude to wavelength ratio [46]. The frequencies of these waves follow a geometric progression and develop a self-similar fractal profile.

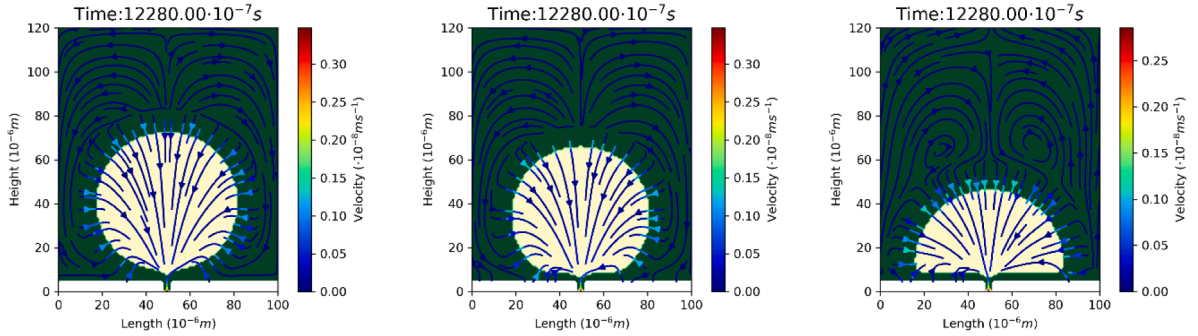


**Fig. 7.** Vapour insertion through an orifice of 5μm for different interface planes: (a) a generic one with specified small contact angle, (b) the $ZrO_2$ $(\bar{1}11)$ surface, (c) the $ZrO_2$ $(001)$ surface. The evolution of the system is greatly affected by the fluid solid interaction at the microscopic level.

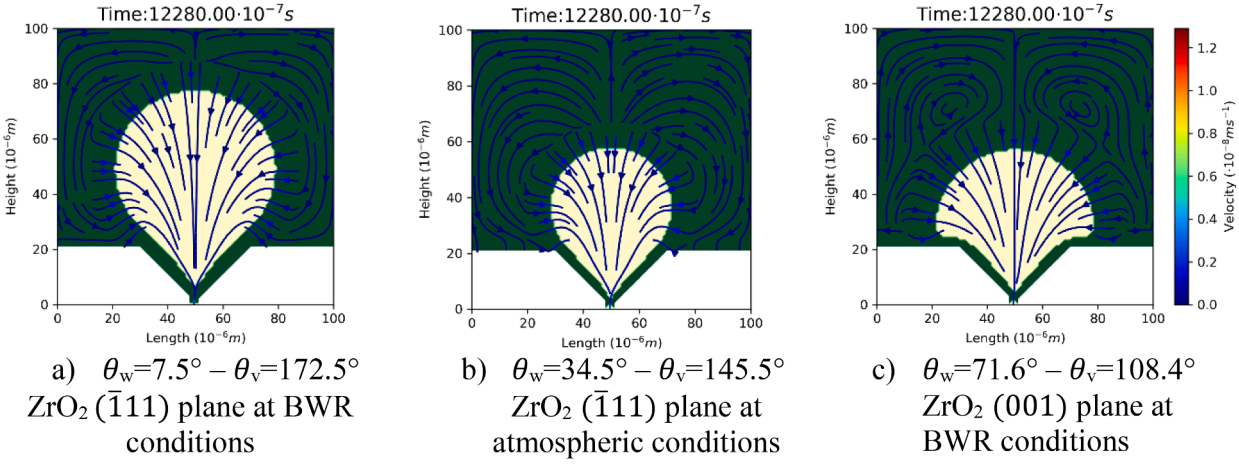


**Fig. 8.** Gas insertion through an inclined 45° orifice for different interface planes in a setup similar to that of Fig. 7: (a) a generic one with specified small contact angle, (b) the $ZrO_2$ $(\bar{1}11)$ surface, (c) the $ZrO_2$ $(001)$ surface. Effect of contact angle on the bubble dynamic evolution is observed.

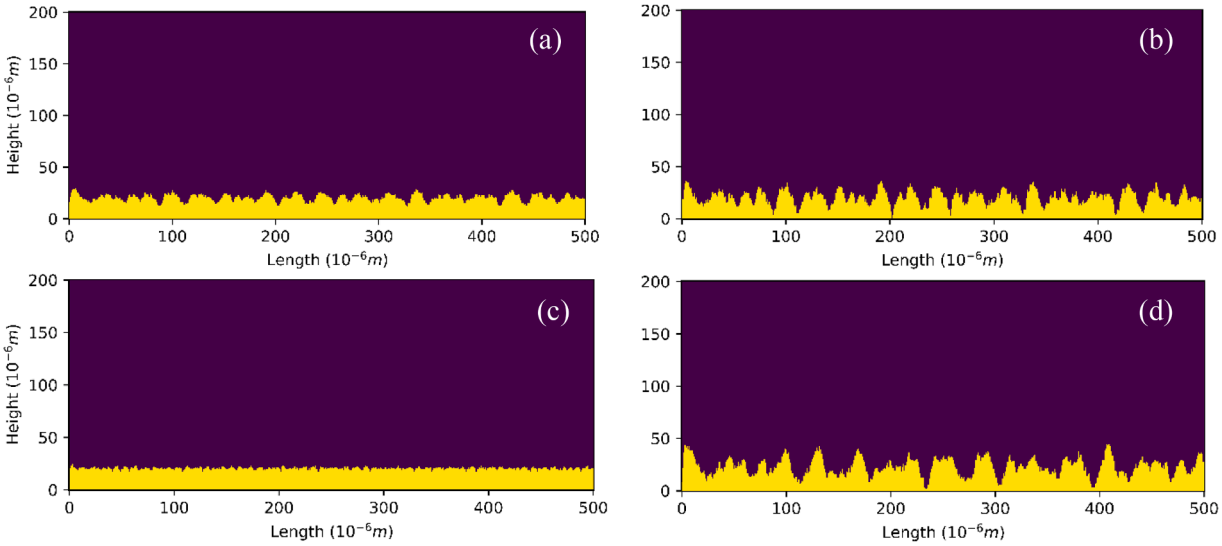


**Fig. 9.** Generated rough surface using the algorithm from [47] with different maximum wavelengths and amplitude to wavelength ratios: (a) Amplitude to wavelength ratio 0.1 and maximum wavelength 20 μm, (b) Amplitude to wavelength ratio 0.2 and maximum wavelength 20 μm, (c) Amplitude to wavelength ratio 0.1 and maximum wavelength 10 μm (d) Amplitude to wavelength ratio 0.1 and maximum wavelength 40 μm.

Fifteen sine waves were used on each occasion, with the geometric progression affected by a random number generator. The generator affects the characteristics of each sine wave such as amplitude and wavelength, with user input defining the limits. The results for all waves are then superimposed to generate a unique profile. Some examples of these profiles can be seen in Fig. 9, where (a) shows an example with amplitude to wavelength ratio of 0.1 and a maximum wavelength of 20 μm, (b) shows a surface with a doubled ratio, (c) with a halved maximum wavelength and (d) with a doubled maximum wavelength. Additional results can be seen in Figs. 10 and 12.

The rough surfaces created are used to investigate the behaviour of a bubble moving above them. This models the flow within the BWR reactor, where the water vapour bubbles, created from the boiling of the cooling water, move upwards along the walls of the fuel containers. Fig. 10 shows two snapshots of the simulation of a bubble with radius 30LU on the same rough surface, characterised by the different contact angles of the plane orientations. The bubble, whose starting coordinates are (0.0075 m, 0.004 m), then moves towards the left. The snapshots in Fig. 10 show the bubble at 3.84 s and at 12.8 s. The movement is considered under the effect of gravity forces, applied on the LB domain towards the negative direction of the length axis, which in the reactor, should cause the bubble to move upwards.

To observe the movement of the bubble within a reasonable computational time (the flow velocity in the previous cases is minimal), we consider the following domain and dimensionalization following the work of [38]: the size of one lattice unit is set as 50 μm (so the bubble radius is 1.5 mm) and the density ratio is now 20. This alters the Eötvös number (using the bubble diameter as characteristic length) to 3.97 when compared to the previous cases. This has a ripple effect to the dimensionalisation of other parameters of the LB simulation. Changes from the LB parameters used in the previous case are shown in Table 2.

The results are in agreement with the behaviour and system evolution as observed in Section 3.5. On the $ZrO_2$ (001) surface, the bubble is trapped not far from its starting position and remains stationary throughout the simulation. This is particularly important because it underlines the possibility of a localised dry-out and a reduction in thermal efficiency. Conversely, the bubble on the $ZrO_2$ ($\bar{1}$11) surface manages to escape from the solid and maintains a distance above the solid, even when it encounters a higher peak, as seen in Fig. 10(a). The bubble subsequently moves above the peak, crossing the periodic boundary and maintaining its height above the surface, as seen in Fig. 10 (b).

### 3.7. Boiling simulations and nucleation site density

The following simulations use the coupled momentum and thermal equation model as presented in Section 2. The simulations in this section use the BWR in-situ operating conditions outlined in Section 3.3 and Table 1 meaning that the simulation begins at boiling conditions. In this simulation gravitational forces are considered. Part of the bottom boundary (the area between 80 and 120LU with the entire domain being 200LU) has been assigned a higher temperature with an overheat of 8°C, a typical overheat temperature, also used in macroscopic simulations focusing on a similar reactor [11,12]. This temperature remains constant and slowly elevates the fluid temperature leading to eventual phase change.

Fig. 11 shows two instances of the bubble created on a flat surface. The gravity vector was modified to reflect different inclined surfaces, however differences in the shape of the emerging bubble (for conditions reflected in Table 1) were not observed. The bubble starts growing in the middle of the heated surface and expands homogeneously in the liquid. The time for the generation of the bubble depends on the overheat applied to the wall, with Fig. 11 showing the generation for 8°C. Detachment of the bubble is not studied within this work, as we focus on the initial formation, but it has already proven possible with different LB models [17,38].

The boiling case was also applied to rough surfaces, created following the same method as in Section 3.6. Unlike the previous case, the elevated temperature is applied to the entirety of the solid surface, to simulate the heated wall within the BWR. The bubble generation is promoted by the breakage in symmetry due to the rough surface which enhances the flow instabilities, compared to the flat wall case, where a homogeneous vapour layer is created if the overheat is applied to the entire boundary.

Fig. 12 shows the results for two $ZrO_2$ rough surfaces with the same wavelength and different amplitudes 12(a) and 12(b), for the two $ZrO_2$

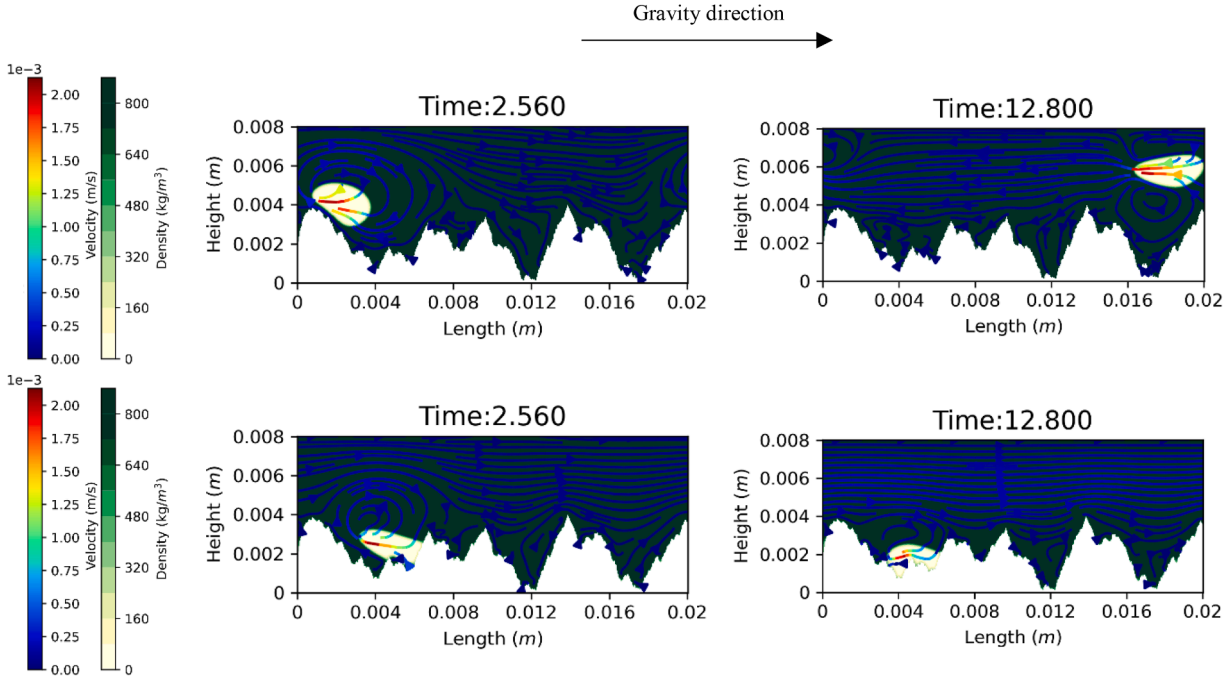


**Fig. 10.** Isothermal bubble flow over a rough surface for the $ZrO_2$ ($\bar{1}$11) at BWR conditions (top) and $ZrO_2$ (001) at BWR conditions (bottom).

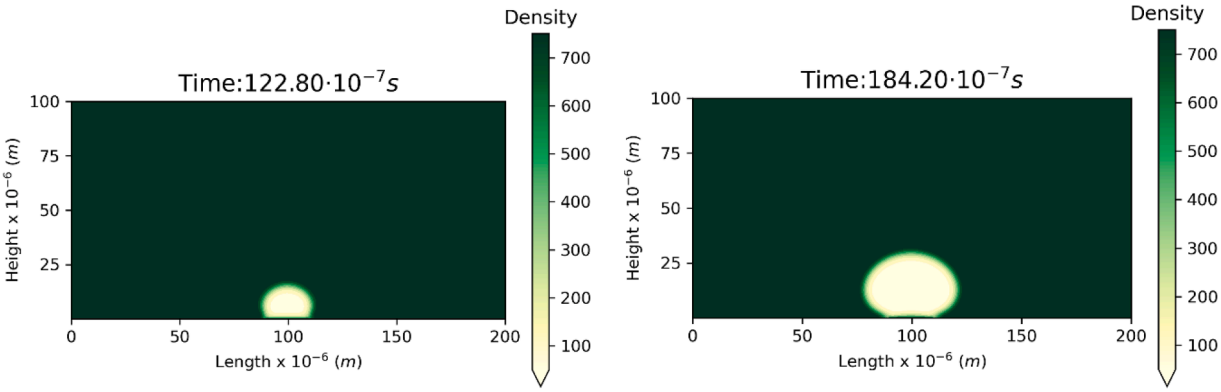


**Fig. 11.** Bubble nucleation over a flat surface for the $ZrO_2$ $(\bar{1}11)$ surface at different times.

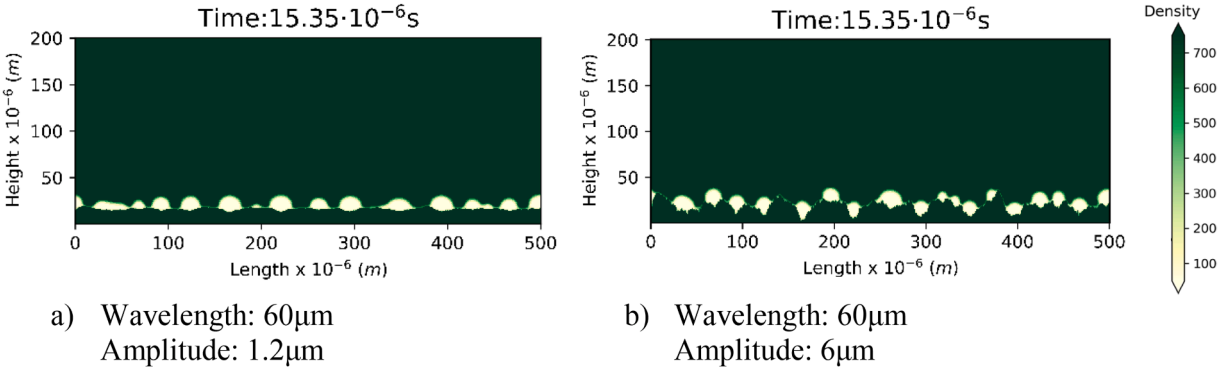


**Fig. 12.** Bubble nucleation over different rough surfaces (left-right) for the $ZrO_2$ (001) plane at BWR conditions.

**Table 2**
Dimensionalisation data for the bubble moving over a rough surface.

| Physical Parameter | Real value | LB Value |
|---|---|---|
| Node distance | $50{\cdot}10^{-6}$m | 1 |
| Eötvös number | 3.97 | 3.97 |
| Gravity Force | $9.81\text{m}^2\text{s}^{-1}$ | $10^{-4}$ |
| Vapour Density | $42.4\text{kgm}^{-3}$ | 0.318 |
| Liquid Density | $848\text{kgm}^{-3}$ | 6.48 |
| Density Ratio | 20 | 20 |

planes (Fig. 12 top and bottom). The change in the surface characteristics leads to the appearance of different numbers of bubbles and at different positions. In particular, Fig. 12(a) has produced 15 bubbles and Fig. 12(b) has produced 18 bubbles for the $ZrO_2$ (001) case. Only bubbles that have reached the 7.7 μm (8LU) radius without merging are considered. These cases use the (001) surface, so the vapour bubbles are in direct contact to the solid surface. Considering the same setup and conditions for the $ZrO_2$ $(\bar{1}11)$ surface at BWR conditions, while we observed an initial drop in density, due the hydrophilic nature of the surface, the lower density fluid was moved away from the surface and bubble formation was not observed until numerical instabilities started to appear. It seems that the current simulation setup (pressure, temperature, hydrophilic surface) was challenging for the specific LB and boundary condition model.

The rough surface boiling simulations were executed for different configurations, in order to measure the number of bubbles generated. The length of the domain was increased four times from the simulation setup of Fig. 12 and 2000LU were used to discretize the domain. This allows to lessen the influence of the finite domain and to improve the statistics relevant to the number of the bubbles generated. Fig. 13 shows the results of the different sets of simulations arranged by the average surface roughness (which is determined also by the amplitude, with a larger amplitude correlating to a larger roughness) and the wavelength itself for the $ZrO_2$ (001) at BWR conditions.

By interpreting the results, we can infer that both the wavelength used for the generation, and the resulting surface roughness, have strong influence on the nucleation site density. Smaller wavelength and higher roughness correlate to the generation of more bubbles. Considering the fractal method used for the surface generation, the wavelength size has a direct impact on its shape; smaller sizes lead to a larger number of troughs and peaks for the generated wave-surface. This increases the contact surface between fluid and the overheated cladding and creates more surfaces where the fluid is surrounded by solid nodes. The effect is exacerbated for larger amplitudes which create surfaces with higher roughness. Both lead to an increase of the heat transfer rate leading to faster temperature changes, a localised drop in density and finally bubble nucleation. Therefore, we can conclude that the surface shape is an important factor in determining nucleation site density.

Moreover, the simulation results have allowed the creation of a correlation between the roughness and the nucleation site density from first principles. These correlations follow the form shown in Eq. (20) with different coefficients $A_1$ and $A_2$ for each wavelength (Table 3) and provide a prediction of the nucleation site density at specific conditions (operating reactor conditions) for $ZrO_2$ (001) surface, provided the details of the surface morphology are known. Additionally, power correlations can be found for results from different wavelengths in a narrow roughness band.

$$\{\textit{Nucleation Site Density}\} = A_1 \cdot e^{A_2 \cdot \{\textit{Surface Roughness Factor}\}} \tag{20}$$

Comparing with the experimental works of [48], the values obtained in this paper are on the same order of magnitude as the experimental, as shown in Fig. 14, with the differences being due to different overheat values (6°C compared to 8°C in this paper) and the use of steel instead of

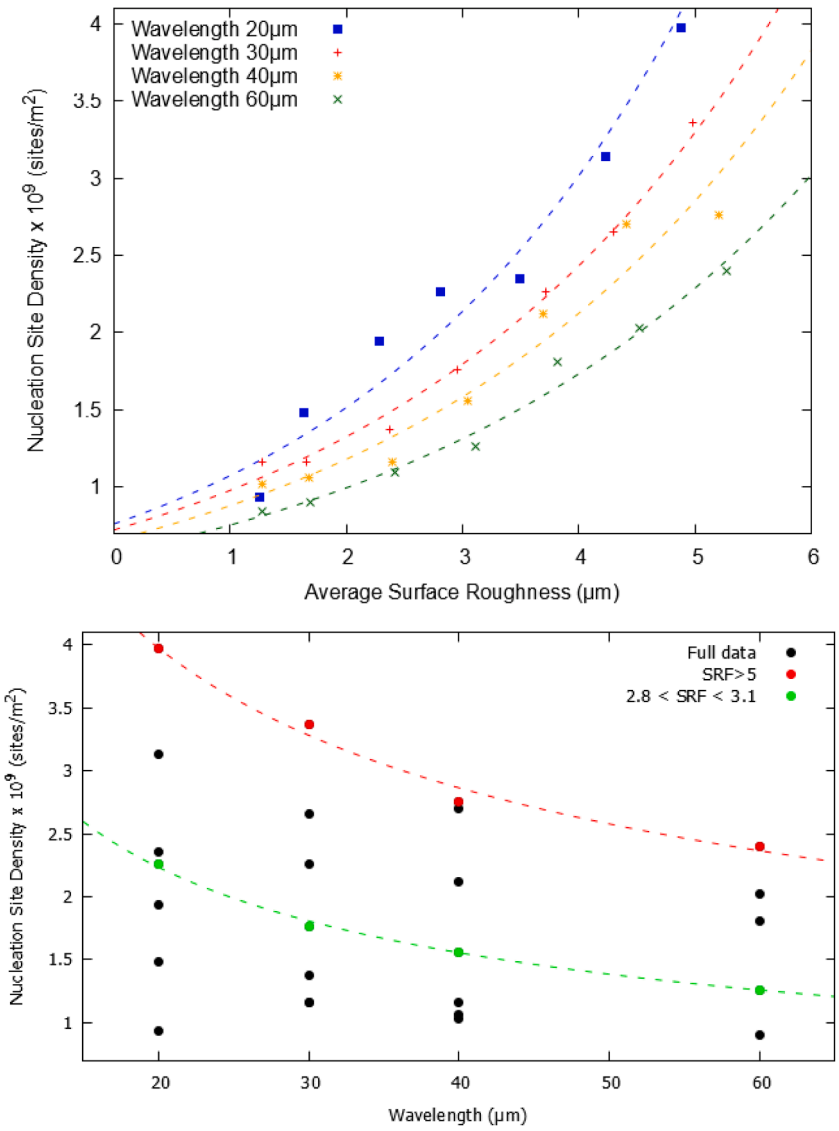


**Fig. 13.** Nucleation site density for different rough surfaces arranged by average surface roughness (top) and rough surface wavelength (bottom) for the $ZrO_2$ (001) surface at BWR conditions. A regression on the simulation results allows to extract correlations linking the nucleation density to surface roughness for each wavelength.

**Table 3**
Coefficients of Eq. (20) for different wavelengths.

| Wavelength (μm) | $A_1$ | $A_2$ | $R^2$ coefficient |
|---|---|---|---|
| 20 | $7.601 \cdot 10^8$ | 0.3446 | 0.9606 |
| 30 | $7.212 \cdot 10^8$ | 0.3040 | 0.9933 |
| 40 | $6.543 \cdot 10^8$ | 0.2945 | 0.9328 |
| 60 | $5.700 \cdot 10^8$ | 0.2780 | 0.9819 |

$ZrO_2$. The values also follow closely the model from Hibiki and Ishii [49]. To expand the values to 3D, the values in Fig. 13 were multiplied to themselves as an upper boundary for the expansion.

It is noted here that the nucleation site density is the key parameter to upscale boiling physics from the surface roughness level (micrometre level) to the continuum scale where the numerical solvers consider the surface roughness in an implicit way. This will conclude the transfer of boiling information from the atomistic scale to the micrometre scale and from the micrometre scale to the reactor scale.

## 4. Conclusions

A LB model was developed for boiling flow simulation over micrometre scale rough surfaces and applied to investigate the relationship between material properties and vapour nucleation at conditions relevant to the operation of BWR. The cladding material was considered to be zirconia for which the two most relevant $ZrO_2$ surfaces, $(\bar{1}11)$ and (001), were considered. MD simulations were used to calculate the contact angles during the nucleate boiling. The contact angle of water for the studied faces $(\bar{1}11)$ and (001) differ by more than 80°. This suggests that at the vapour-fluid-solid interactions are strongly dependent on the surface structure of the cladding material.

In the applied multiscale modelling approach, the contact angle calculated by molecular simulations is the effective coupling parameter between the nanoscale molecular interaction at the interface and the boundary condition at microscale by implementing in the 2D LB simulation. The effect of the different contact angles was demonstrated in both dynamic and static cases. For the lower contact angle for the (001) plane, the bubble remained close to the surface for longer periods compared to the $(\bar{1}11)$ surface, showcasing a reason for probable

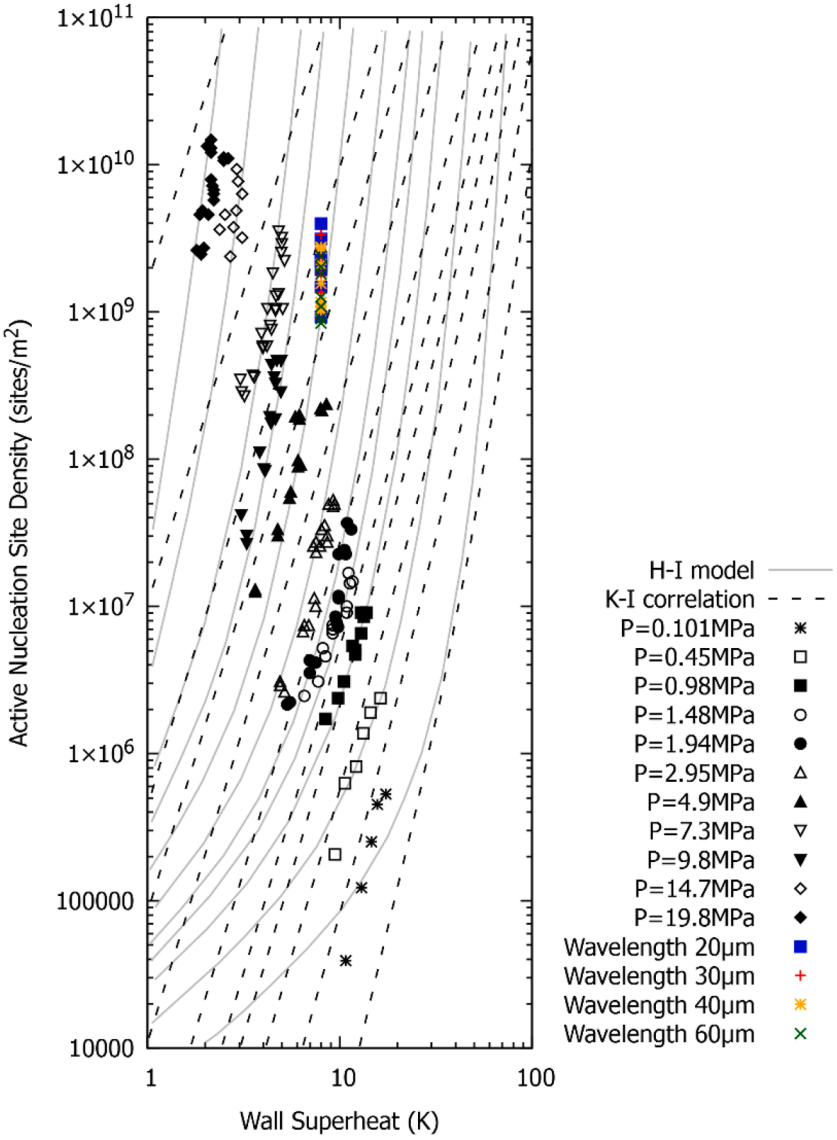


**Fig. 14.** Nucleation site density comparison between the LB results in this report, the experimental results of Borishanskii et al. [48], the model by Hibiki and Ishii [49] and the correlation of Kocamustafaogullari and Ishii [9]. Values from this paper are added in colour, with only the highest and lowest values from Fig. 13 being added for clarity. To transfer the values to 3D, the values in Fig. 13 were multiplied by themselves.

localised dry outs and lower thermal efficiency in the FA system.

An additional thermodynamic model for the energy equation was implemented in the LB code and benchmarked. It was used to investigate nucleate boiling on the zirconia surface, both on a flat and on an algorithmically generated rough surface. The latter provided information on the nucleation site density for different surfaces. The shape of the surface and the surface roughness were found to have a significant effect with higher roughness and smaller wavelengths leading to more bubbles generated. The results were in line with experimental results for similar pressure.

This work provides a methodology for coupling boiling modelling across different length and time scales. The bottom-up approach starts from fundamental principles of interatomic interaction allowing the systematic investigations of the boiling phenomena on different material surface in the microscale. In the chain of models, the nucleation site density is then the upscaling parameter from microscopic simulations to continuum scale simulations. The microscopic LB results can therefore be upscaled to the macroscale FEM simulations for the modelling of the flow by considering the full FA geometry [11]. It also provides a way to produce empirical correlations based on modelling at conditions were experiments are very difficult to conduct.

The accuracy of predictions could be improved in the future by considering a 3D LB simulation and explicit X-ray tomographs / surface roughness of the actual cladding surfaces. Additional wall superheat temperatures can also be examined. The results can be compared to more semi-empirical equations for the nucleation site density and the effect on macroscopic boiling FA simulations could be also investigated. Obtaining the latter can serve as an input to macroscale CFD methods, making a cross-scale simulation of the FA system possible.

## CRediT authorship contribution statement

**A. Mokos:** Methodology, Investigation, Software, Validation, Visualization, Writing – original draft. **R.A. Patel:** Methodology, Investigation, Software, Writing – review & editing. **K. Karalis:** Methodology, Investigation, Software, Visualization, Writing – original draft. **S.V. Churakov:** Supervision, Project administration, Writing – review & editing. **N.I. Prasianakis:** Conceptualization, Supervision, Project administration, Writing – review & editing, Funding acquisition.

## Declaration of competing interest

The authors declare that they have no known competing financial interests or personal relationships that could have appeared to influence the work reported in this paper.

## Data availability

Data will be made available on request.

## Acknowledgments

The authors would like to acknowledge the assistance of Dr. Y. Sato and Dr. B. Niceno in identifying the conditions within a BWR and leading the LSM_20_02 and LSM_22_02 projects. The authors would like to thank Swissnuclear for providing funding for this research under the projects LSM_20_02 and LSM_22_02. We would also like to thank the CSCS Swiss National Supercomputing Centre for providing the computational facilities for the simulations in this work under the project s1155.

## Appendix A. LB thermal model validations

The first case to be investigated is an unsteady conjugate heat conduction problem [50], which is shown in Fig. 15. The domain consists of three fluids with different thermal conductivities $\kappa$ and diffusivities $\alpha$ with a temperature difference between the bottom and top boundaries. The fluids remain still and only the energy equation is solved with the LB code. Gravitational force is not implemented in this benchmark. The results, as demonstrated in Fig. 15, show the evolution over time of the dimensionless temperature $\theta$ across the vertical axis of the domain. The temperature profile, initially set to $\theta = 0$ for all fluids, evolves in three linear gradients, depending on the fluid characteristics. The results are compared with the analytical solution [51] and show that the model simulates accurately the transient thermal flow. Each fluid consisted of 150 points across the vertical direction.

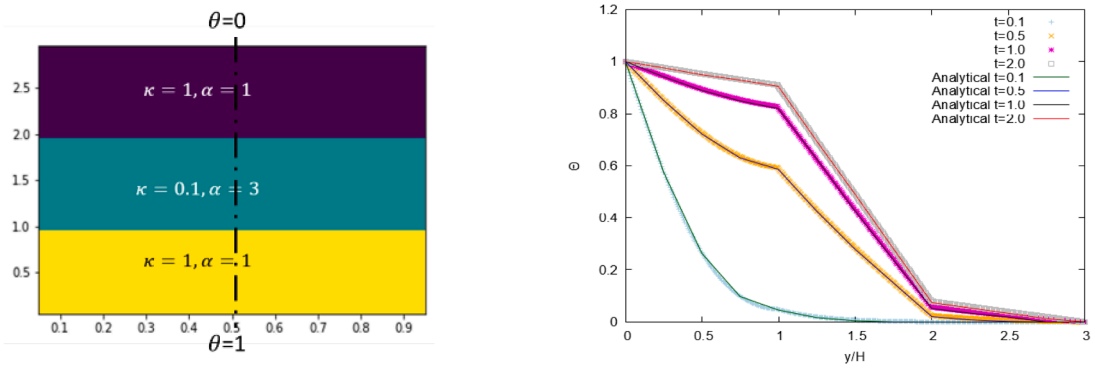


**Fig. 15.** LB results for a conjugate unsteady heat conduction problem (middle), compared to analytical results [51] (right). Solid lines represent the analytical solution and symbols the simulation results at different time steps.

An additional benchmark is provided by [52], looking at Rayleigh-Bernard convection with conjugate heat transfer. The domain, shown in Fig. 15, consists of a solid wall on the left boundary interfacing with a fluid. A temperature difference is imposed between the left and right boundaries, while the top and bottom have a zero thermal gradient. The fluid is initially still but is allowed to move under the effect of gravity and thermal convection.

Both the energy and momentum equations are simulated. Fig. 16 shows the contours for the dimensionless velocity and temperature of the fluid at steady state after $0.165ms$. The value of the Nusselt number, which is the ratio of heat transferred by convection versus pure conduction, averaged on the solid surface can then be found by integrating the local heat flux [52]. The value obtained with the current method at steady state is 8.82 on a $225\times225$ lattice grid, which is an error of 2.1 % to the reference value of 9.01 [52].

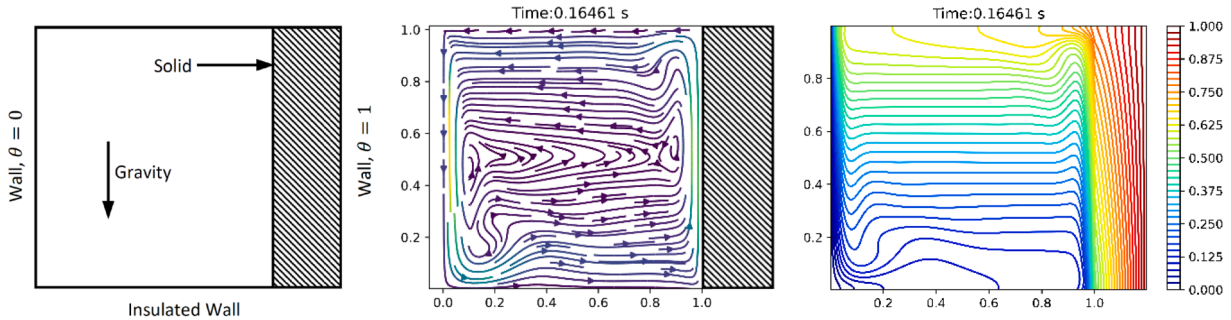


**Fig. 16.** LB results for a conjugate heat transfer problem (left), showing the dimensionless velocity (middle) and temperature contours (right).

## Appendix B. Grid refinement study

We have investigated the effect of a more refined grid on the simulation results. The case shown in Fig. 11, bubble nucleation over a flat surface was investigated. The distance between nodes (finer spatial discretization) was reduced to half, corresponding to a change of the spatial grid resolution from $\Delta x = 10^{-6}m$ to $\Delta x = 5{\cdot}10^{-7}m$. To maintain the same conditions, the dimensionless numbers mentioned in Eq. (18) are kept constant. This is particularly relevant for the Laplace and Eötvös numbers as they depend on the characteristic length. Following [53], we considered the density ratio

to be constant and the surface tension (in lattice Boltzmann units, and to keep the dimensionless numbers same) to linearly change with the node distance. This allows us to recalculate the LB units, and the gravity through the Eötvös number with the new LB value being $1.15{\cdot}10^{-9}$. The time step can then be adjusted accordingly.

The result of the refined simulation is shown on the right of Fig. 17 and is compared to the original simulation on the left. The bubbles produced grow to an extremely similar shape at the same time, with the only difference being a sharper interface for the refined grid, which is expected. We can then conclude that the resolution used in the main part of the work is sufficient.

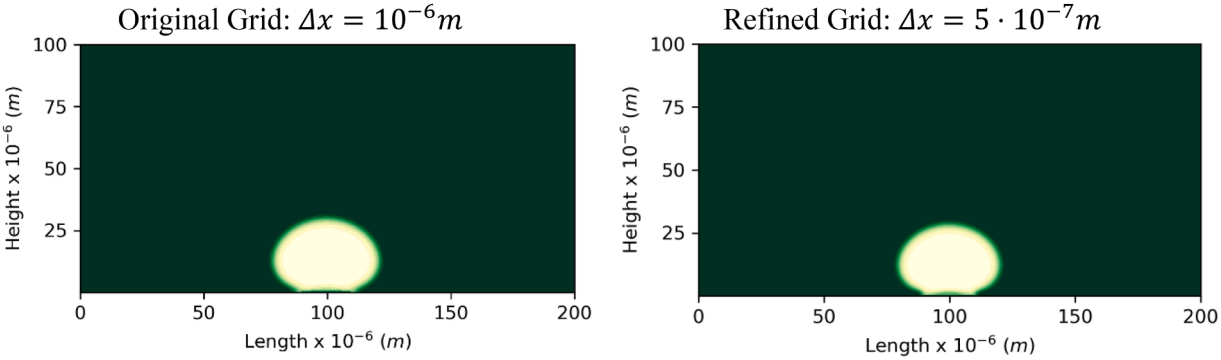


**Fig. 17.** LB results for a bubble nucleating on a flat surface for different grids, original (left) and refined (right) *at* $184{\cdot}10^{-7}$s.

## References


[1] L.S. Tong, J. Weisman, Thermal analysis of pressurized water reactors, American Nuclear Society, United States, 1995.
[2] EPRI, PWR Axial Offset Anomaly (AOA) Guidelines, Revision 1, EPRI, Palo Alto, California, 2004. No. 1008102.
[3] EPRI, Modeling PWR Fuel Corrosion Product Deposition and Growth Processes, EPRI, Palo Alto, California, 2004. No. 1009734.
[4] IAEA, Review of Fuel Failures in Water Cooled Reactors, International Atomic Energy Agency, 2010. Technical Report.
[5] J. Buongiorno, Can corrosion and CRUD actually improve safety margins in LWRs? Ann. Nucl. Energy 63 (2014) 9–21.
[6] Banerjee, S., 2001, "Nuclear applications: zirconium alloys," pp. 6287-6299.
[7] R. Hernandez, C.P. Folsom, N.E. Woolstenhulme, C.B. Jensen, J.D. Bess, J. P. Gorton, N.R. Brown, Review of pool boiling critical heat flux (CHF) and heater rod design for CHF experiments in TREAT, Prog. Nucl. Energy 123 (2020) 103303.
[8] I. Dumnernchanvanit, N.Q. Zhang, S. Robertson, A. Delmore, M.B. Carlson, D. Hussey, M.P. Short, Initial experimental evaluation of crud-resistant materials for light water reactors, J. Nucl. Mater. 498 (2018) 1–8.
[9] G. Kocamustafaogullari, M. Ishii, Interfacial area and nucleation site density in boiling systems, Int. J. Heat Mass Trans. 26 (9) (1983) 1377–1387.
[10] G. Giustini, Modelling of boiling flows for nuclear thermal hydraulics applications—a brief review, Inventions 5 (3) (2020) 47.
[11] Y. Sato, B. Niceno, Pool boiling simulation using an interface tracking method: From nucleate boiling to film boiling regime through critical heat flux, Int. J. Heat Mass Trans. 125 (2018) 876–890.
[12] Y. Sato, B. Niceno, Nucleate pool boiling simulations using the interface tracking method: boiling regime from discrete bubble to vapor mushroom region, Int. J. Heat Mass Trans. 105 (2017) 505–524.
[13] K. Karalis, D. Zahn, N. Prasianakis, B. Niceno, S.V. Churakov, Deciphering the molecular mechanism of water boiling at heterogeneous interfaces, Sci. Rep-Uk 11 (19858) (2021).
[14] C. Dellago, P.G. Bolhuis, D. Chandler, Efficient transition path sampling: application to Lennard-Jones cluster rearrangements, J. Chem. Phys. 108 (22) (1998) 9236–9245.
[15] H. Huang, M.C. Sukop, X.Y. Lu, Multiphase Lattice Boltzmann Methods: Theory and Application, John Wiley & Sons, Ltd, 2015.
[16] M.J. Krause, A. Kummerländer, S.J. Avis, H. Kusumaatmaja, D. Dapelo, F. Klemens, M. Gaedtke, N. Hafen, A. Mink, R. Trunk, J.E. Marquardt, M.L. Maier, M. Haussmann, S. Simonis, OpenLB—Open source lattice Boltzmann code, Comput. Math. Appl. 81 (2021) 258–288.
[17] Q. Li, K.H. Luo, Q.J. Kang, Y.L. He, Q. Chen, Q. Liu, Lattice Boltzmann methods for multiphase flow and phase-change heat transfer, Prog. Energy Combust. Sci. 52 (2016) 62–105.
[18] S. Plimpton, Fast parallel algorithms for short-range molecular dynamics, J. Comput. Phys. 117 (1) (1995) 1–19.
[19] L.R. Martins, M.S. Skaf, B.M. Ladanyi, Solvation dynamics at the water/zirconia interface: molecular dynamics simulations, J. Phys. Chem. B 108 (51) (2004) 19687–19697.
[20] K. Karalis, D. Zahn, N.I. Prasianakis, B. Niceno, S.V. Churakov, Deciphering the molecular mechanism of water boiling at heterogeneous interfaces, Sci. Rep-Uk 11 (1) (2021).
[21] A. Christensen, E.A. Carter, First-principles study of the surfaces of zirconia, Phys. Rev. B 58 (12) (1998) 8050.
[22] D. Surblys, F. Leroy, Y. Yamaguchi, F. Müller-Plathe, Molecular dynamics analysis of the influence of Coulomb and van der Waals interactions on the work of adhesion at the solid-liquid interface, J. Chem. Phys. 148 (13) (2018) 134707.
[23] Patel, R. A., 2022, "Yantra Git repository," https://bitbucket.org/yantralb m/yantra.
[24] Y.H. Qian, D. d'Humières, P. Lallemand, Lattice BGK models for Navier-Stokes equation, EPL (Europhys. Lett.) 17 (6) (1992) 479.
[25] P. Lallemand, L.S. Luo, Theory of the lattice Boltzmann method: dispersion, dissipation, isotropy, Galilean invariance, and stability, Phys. Rev. E 61 (6) (2000) 6546–6562.
[26] D.A. Wolf-Gladrow, Lattice-gas cellular automata and lattice Boltzmann models - introduction, Lect. Notes Math 1725 (2000) 1–13.
[27] M.E. McCracken, J. Abraham, Multiple-relaxation-time lattice-Boltzmann model for multiphase flow, Phys. Rev. E 71 (3) (2005).
[28] I. Ginzburg, Equilibrium-type and link-type lattice Boltzmann models for generic advection and anisotropic-dispersion equation, Adv. Water. Resour. 28 (11) (2005) 1171–1195.
[29] I. Ginzburg, D. d'Humières, A. Kuzmin, Optimal stability of advection-diffusion lattice Boltzmann models with two relaxation times for positive/negative equilibrium, J. Stat. Phys. 139 (6) (2010) 1090–1143.
[30] L.S. Luo, Unified theory of lattice Boltzmann models for nonideal gases, Phys. Rev. Lett. 81 (8) (1998) 1618–1621.
[31] X.W. Shan, H.D. Chen, Lattice Boltzmann model for simulating flows with multiple phases and components, Phys. Rev. E 47 (3) (1993) 1815–1819.
[32] X.W. Shan, H.D. Chen, Simulation of nonideal gases and liquid-gas phase-transitions by the lattice Boltzmann-Equation, Phys. Rev. E 49 (4) (1994) 2941–2948.
[33] X.Y. He, G.D. Doolen, Thermodynamic foundations of kinetic theory and lattice Boltzmann models for multiphase flows, J. Stat. Phys. 107 (1-2) (2002) 309–328.
[34] D. Peng, D.B. Robinson, A new two-constant equation of state, Ind. Eng. Chem. Fund. 15 (1) (1976) 59–64.
[35] P. Yuan, L. Schaefer, Equations of state in a lattice Boltzmann model, Phys. Fluids 18 (4) (2006) 042101.
[36] X.W. Shan, G. Doolen, Multicomponent Lattice-Boltzmann Model with Interparticle Interaction, J. Stat. Phys. 81 (1-2) (1995) 379–393.
[37] Patel, R., 2016, "Lattice Boltzmann method based framework for simulating physico-chemical processes in heterogeneous porous media and its application to cement paste".
[38] Q. Li, Q.J. Kang, M.M. Francois, Y.L. He, K.H. Luo, Lattice Boltzmann modeling of boiling heat transfer: the boiling curve and the effects of wettability, Int. J. Heat Mass Trans. 85 (2015) 787–796.
[39] L.K. Li, R.W. Mei, J.F. Klausner, Lattice Boltzmann models for the convection-diffusion equation: D2Q5 vs D2Q9, Int. J. Heat Mass Trans. 108 (2017) 41–62.
[40] E.G. Flekkøy, Lattice Bhatnagar-Gross-Krook models for miscible fluids, Phys. Rev. E 47 (6) (1993) 4247–4257.
[41] R.A. Patel, J. Perko, D. Jacques, G. De Schutter, K. Van Breugel, G. Ye, A versatile pore-scale multicomponent reactive transport approach based on lattice Boltzmann method: application to portlandite dissolution, Phys. Chem. Earth 70-71 (2014) 127–137.
[42] I.H. Bell, J. Wronski, S. Quoilin, V. Lemort, Pure and Pseudo-pure Fluid Thermophysical Property Evaluation and the Open-Source Thermophysical Property Library CoolProp, Ind. Eng. Chem. Res. 53 (6) (2014) 2498–2508.
[43] R. Benzi, L. Biferale, M. Sbragaglia, S. Succi, F. Toschi, Mesoscopic modeling of a two-phase flow in the presence of boundaries: the contact angle, Phys. Rev. E 74 (2) (2006) 021509.

[44] B.H. Wen, B.F. Huang, Z.R. Qin, C.L. Wang, C.Y. Zhang, Contact angle measurement in lattice Boltzmann method, Comput. Math. Appl. 76 (7) (2018) 1686–1698.
[45] F. Qin, J. Zhao, Q. Kang, D. Derome, J. Carmeliet, Lattice Boltzmann modeling of drying of porous media considering contact angle hysteresis, Transport Porous Med. 140 (1) (2021) 395–420.
[46] W.L. Power, T.E. Tullis, Euclidean and fractal models for the description of rock surface-roughness, J. Geophys. Res-Solid 96 (B1) (1991) 415–424.
[47] H. Deng, S. Molins, D. Trebotich, C. Steefel, D. DePaolo, Pore-scale numerical investigation of the impacts of surface roughness: upscaling of reaction rates in rough fractures, Geochim. Cosmochim. Ac 239 (2018) 374–389.
[48] Borishanskiĭ, V. M., Bobrovich, G. I., and Minchenko, F. P., 1969 "7 – Heat transfer from a tube to water and to ethanol in nucleate pool boiling".
[49] T. Hibiki, M. Ishii, Active nucleation site density in boiling systems, Int. J. Heat Mass Trans. 46 (2003) 2587–2601.
[50] H. Karani, C. Huber, Lattice Boltzmann formulation for conjugate heat transfer in heterogeneous media, Phys. Rev. E 91 (2) (2015) 023304.
[51] Y.Z. Sun, I.S. Wichman, On transient heat conduction in a one-dimensional composite slab, Int. J. Heat Mass Trans. 47 (6-7) (2004) 1555–1559.
[52] X. Pan, C. Lee, J.I. Choi, Efficient monolithic projection method for time-dependent conjugate heat transfer problems, J. Comput. Phys. 369 (2018) 191–208.
[53] A. Jaramillo, V. Pessoa Mapelli, L. Cabezas-Gómez, Pseudopotential lattice Boltzmann method for boiling heat transfer: a mesh refinement procedure, Appl. Therm. Eng. 213 (2022) 118705.